Redox Biology 59 (2023) 102550

Contents lists available at ScienceDirect

Redox Biology

journal homepage: www.elsevier.com/locate/redox

Neuronal deletion of MnSOD in mice leads to demyelination, inflammation and progressive paralysis that mimics phenotypes associated with progressive multiple sclerosis

Shylesh Bhaskaran [a], Gaurav Kumar [b], Nidheesh Thadathil [d], Katarzyna M. Piekarz [a], Sabira Mohammed [e], Sergio Dominguez Lopez [a], Rizwan Qaisar [a], Dorothy Walton [a], Jacob L. Brown [a,f], Ashley Murphy [a], Nataliya Smith [c], Debra Saunders [c], Michael J. Beckstead [a,f], Scott Plafker [a], Tommy L. Lewis Jr. [a], Rheal Towner [c], Sathyaseelan S. Deepa [d,e], Arlan Richardson [d,e,f], Robert C. Axtell [b,**], Holly Van Remmen [a,f,*]

[a] Aging & Metabolism Research Program, Oklahoma Medical Research Foundation, OK, USA
[b] Arthritis & Clinical Immunology, Oklahoma Medical Research Foundation, OK, USA
[c] Advanced Magnetic Resonance Center, Oklahoma Medical Research Foundation, OK, USA
[d] Department of Biochemistry and Molecular Biology, University of Oklahoma Health Sciences Center, OK, USA
[e] Stephenson Cancer Center, University of Oklahoma Health Sciences Center, Oklahoma City, OK, USA
[f] Oklahoma City VA Medical Center, Oklahoma City, OK, USA

ARTICLE INFO

Keywords:
Mn superoxide dismutase
Neurons
Demyelination
Mitochondria
Multiple sclerosis
Necroptosis
Inflammation

ABSTRACT

Neuronal oxidative stress has been implicated in aging and neurodegenerative disease. Here we investigated the impact of elevated oxidative stress induced in mouse spinal cord by deletion of Mn-Superoxide dismutase (MnSOD) using a neuron specific Cre recombinase in *Sod2* floxed mice (i-mn-*Sod2* KO). *Sod2* deletion in spinal cord neurons was associated with mitochondrial alterations and peroxide generation. Phenotypically, i-mn-*Sod2* KO mice experienced hindlimb paralysis and clasping behavior associated with extensive demyelination and reduced nerve conduction velocity, axonal degeneration, enhanced blood brain barrier permeability, elevated inflammatory cytokines, microglia activation, infiltration of neutrophils and necroptosis in spinal cord. In contrast, spinal cord motor neuron number, innervation of neuromuscular junctions, muscle mass, and contractile function were not altered. Overall, our findings show that loss of MnSOD in spinal cord promotes a phenotype of demyelination, inflammation and progressive paralysis that mimics phenotypes associated with progressive multiple sclerosis.

1. Introduction

Oxidative stress is implicated in the initiation and progression of a number of neurodegenerative diseases including Alzheimer's disease (AD) [1] Parkinson's disease (PD) [2] and multiple sclerosis (MS), an inflammatory, demyelinating disease of the central nervous system [3,4]. Neurons are particularly sensitive to changes in oxidative stress, likely because they are postmitotic, have critical energy demands and high concentrations of polyunsaturated fatty acids in their membranes that can be easily altered by oxidation [5].

MnSOD encoded by the *Sod2* gene is a critical component of mitochondrial and cellular maintenance of redox homeostasis and protects cells from oxidative stress. Several studies show severe and lethal phenotypes associated with germline deletion of the *Sod2* gene, where mice have multi-organ dysfunction and do not survive beyond 10–21 days depending on the genetic background [6–8].

For this study, our goal was to determine the neuronal specific function of *Sod2* in adult mice. To circumvent the neonatal lethality of germline *Sod2* knockout mice and to determine the function of *Sod2* in motor neurons, we generated an inducible motor neuron *Sod2*KO (i-mn-*Sod2* KO) mouse [9] by crossing *Sod2* floxed mice with a tamoxifen inducible neuronal specific Cre mouse, SLICK-H Cre [10]. For these

* Corresponding author. Aging and Metabolism Research Program, Oklahoma Medical Research Foundation, 825 NE 13th Street, Oklahoma City, OK, 73104, USA.
** Corresponding author. Arthritis & Clinical Immunology,Oklahoma Medical Research Foundation, 825 NE 13th Street, Oklahoma City, OK, 73104, USA.
E-mail addresses: bob-axtell@omrf.org (R.C. Axtell), Holly-VanRemmen@omrf.org (H. Van Remmen).

https://doi.org/10.1016/j.redox.2022.102550
Received 17 October 2022; Received in revised form 17 November 2022; Accepted 21 November 2022
Available online 26 November 2022

experiments, *Sod2* was deleted in the i-mn-*Sod2* KO mice by tamoxifen injection at 2–3 months of age. By 8 months of age, the i-mn-*Sod2* KO mice exhibited neuronal deficits which resulted in dysfunction of motor coordination. The neurological dysfunction was associated with an increased inflammatory response, loss of myelination and infiltration of immune cells, i.e., phenotypes that are associated with multiple sclerosis (MS).

2. Results

2.1. Generation and characterization of i-mn-Sod2 KO mice

The Slick-H Cre mouse was originally developed as a model to delete genes in neurons while simultaneously labeling the neurons with YFP (*10*). Crossing Slick-H Cre mice with mice carrying the *Sod2* floxed allele ($Sod2^{flox/flox}$; Slick-H Cre^{pos}) followed by tamoxifen treatment resulted in *Sod2* gene excision from motor neurons, and motor neuron targeted expression of YFP (i-mn-*Sod2* KO mice). The $Sod2^{flox/flox}$; Slick-H Cre^{pos} mice were injected at 2–3 months of age with tamoxifen, and changes in body weight, fat mass and lean mass were assessed monthly. No change in either body weight, lean or fat mass was observed until 7 months of age (i.e., 4–5 months after tamoxifen injection). However, at 8 months of age (~5 months after tamoxifen injection) a significant reduction in fat mass was observed in i-mn-*Sod2* KO mice with no difference in either lean mass or body weight (Figs. S1A–C).

To confirm the extent and specificity of *Sod2* deletion to neuronal tissue, we measured protein levels of MnSOD in neuronal tissues (cortex, spinal cord, and sciatic nerve) and non-neuronal tissues (gastrocnemius and spleen) of control ($Sod2^{flox/flox}$; SlickH-Cre^{neg}) and i-mn-*Sod2* KO mice ($Sod2^{flox/flox}$; Slick-H-Cre^{pos}) injected with tamoxifen. MnSOD protein level was reduced in brain (~65.25%), spinal cord (~61.38%), and sciatic nerve (~73.65%) of i-mn-*Sod2* KO mice, compared to age-matched control mice, while MnSOD protein levels in gastrocnemius muscle and spleen remain unchanged (Figs. S2A–E). The reduction of MnSOD in neuronal tissues did not result in a compensatory increase in the levels of CuZn Superoxide Dismutase (CuZnSOD) (data not shown). Generation of i-mn-*Sod2* KO mouse model and the timeframe for different functional analyses are schematically represented in Fig. 1.

2.2. Absence of Sod2 in motor neurons causes defects in locomotor activity and vision

Two months after tamoxifen induced deletion of MnSOD in neurons, mice began to display a number of motor phenotypes (Fig. 2) and by five months post deletion, i-mn-*Sod2* KO animals and exhibited full hindlimb paralysis (Movie S1). Specifically, we found that stride length, measured using the footprint test, showed a significant reduction (~50%) in the i-mn-*Sod2* KO mice compared to control mice (Fig. 2A). In addition, i-mn-*Sod2* KO mice displayed a classical hindlimb clasping, an indicator of motor dysfunction [11], whereas the control mice exhibited normal extension of the hindlimb reflex (Fig. 2B). This phenotype resembles the clinical signs of the experimental autoimmune encephalomyelitis (EAE) model, a well-established neuro-autoimmune model of MS.

Supplementary data related to this article can be found at https://doi.org/10.1016/j.redox.2022.102550.

To further characterize the motor function deficits, we used the open field test [12], which is commonly used to assess locomotion and anxiety [13,14]. Deletion of *Sod2* in motor neurons was associated with a reduction of spontaneous behavioral activity when the animals were tested in an open field (Fig. 2C). The total distance traveled by i-mn-*Sod2* KO mice during the 30-min duration of the test was less than that recorded for in control mice [t (6) = 3.79, p = 0.009]. Additionally, the average duration of immobility episodes was longer in i-mn-*Sod2* KO mice, [t (6) = 3.2, p = 0.018], however, the number of immobility episodes was not different between genotypes (Control = 112.2 ± 13.5; i-mn-*Sod2* KO = 129.5 ± 12.9 t (6) = 0.92, p = 0.4). We further observed a decrease in average speed movement in i-mn-*Sod2* KO mice was observed, compared to control mice [t (6) = 3.78, p = 0.009)]. These findings suggest that the deficiency of neuronal MnSOD in i-mn-*Sod2* KO mice profoundly affected locomotor activity.

The motor deficits observed in the i-mn-*Sod2* KO mice were similar to the clinical signs of the EAE model. We and others have reported that mice with EAE exhibits visual pathology [15]. Therefore, we determined if the i-mn-*Sod2* KO mice have impaired vision. To test whether i-mn-*Sod2* KO mice have visual deficits, we measured visual acuity by optokinetic tracking (OKT). Visual acuity was monitored every month starting 1 month after tamoxifen injection and continued for 5 months. The change in visual acuity was similar in i-mn-*Sod2* KO mice and control mice until 4 months after tamoxifen injection. However, 5 months after tamoxifen injection a significant reduction (~75%) in visual acuity was observed in the left eye (affected eye) of i-mn-*Sod2* KO mice, whereas such an effect was not observed in the right eye (unaffected eye) (Fig. 5A and B). This monocular loss of vision is characteristic of the EAE model [15].

2.3. Absence of Sod2 in neurons does not alter neuromuscular junctions (NMJ), innervation, muscle mass or force generation

NMJs are specialized peripheral synapses between motor neurons and skeletal muscle that allow the nerve transmissions between the skeletal muscle and motor neurons. Previously, we have shown that the absence of CuZnSOD (*Sod*) in neurons leads to muscle atrophy, NMJ disruption, reduced motor neuron number, and reduced muscle force generation in aged mice. In contrast, following *Sod2* deletion, immunofluorescent analysis of the lumbar region of spinal cord indicates there was no change in number of motor neurons numbers (Fig. S3 A). Several studies have shown that NMJ fragmentation is associated with muscle weakness and atrophy. In the present study, deletion of *Sod2* did not change the NMJ morphology or increase fragmentation and muscle mass or contractile functionality (Fig. S3 B-D).

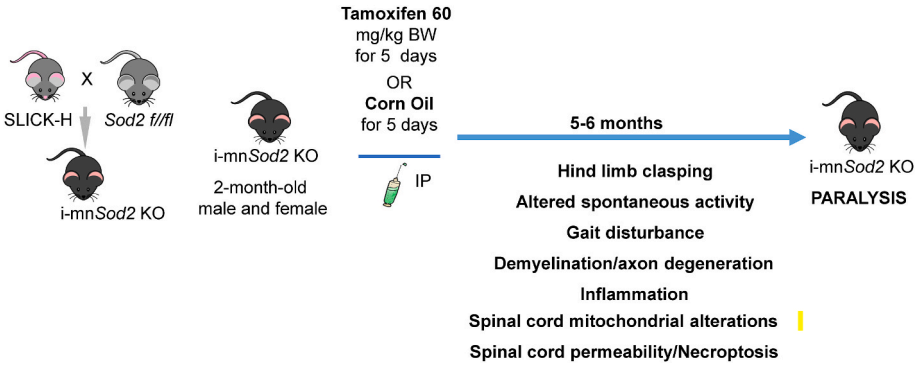

Fig. 1. Study design. Graphical representation of i-mn-*Sod2* KO mouse model generation, outcome measures performed, and the timeframe for function analyses.

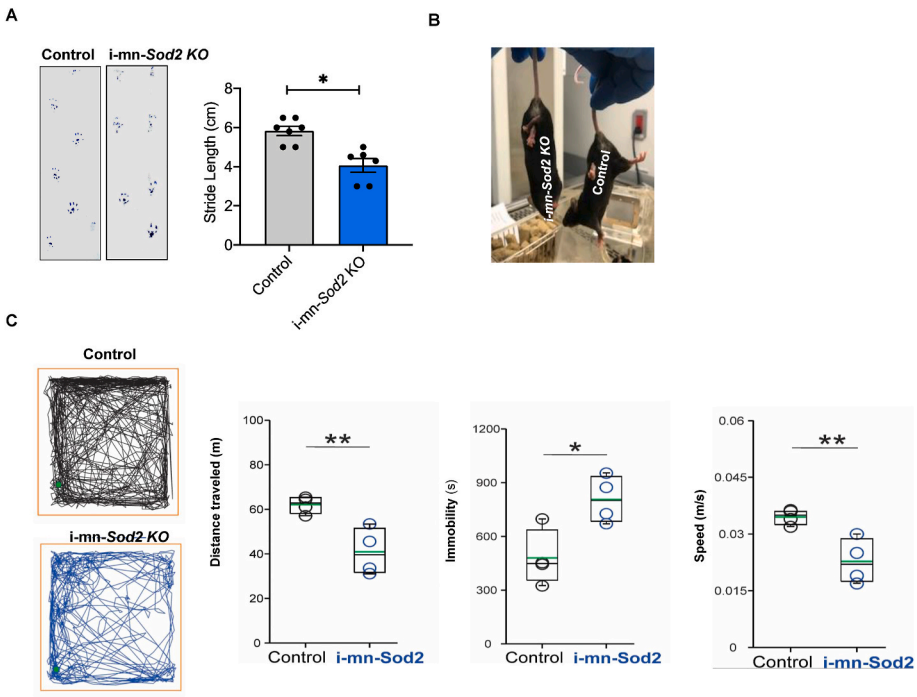

Fig. 2. i-mn-*Sod2* KO mice display gait disturbances, uncoordinated motor activity and decreased spontaneous locomotor activity. A. *Left panel:* Gait analysis assessed by measuring the walking pattern after applying ink to the paws of the mice (left panel). Data shown are from control (grey bar) and i-mn-*Sod2* KO (blue bar) mice at the age of 7 months (i.e., 3–4 months post tamoxifen). *Right panel:* Quantification of stride length. Error bars represent average ± SEM (n = 6–7) student T-test; *P ≤ 0.05. **B.** Representative image of hind limbs clasping phenotype in i-mn-*Sod2* KO mice. Compared to control mice, the i-mn-*Sod2* KO mice exhibit gait changes and clasping behavior. **C.** Representative images of locomotor trajectory from both genotypes for the duration of the test. i-mn-*Sod2* KO mice have a visible decrease in spontaneous locomotion with a less linear pattern. The green dots indicate the initial position of the mice. The total distance traveled was shorter in i-mn-*Sod2* KO mice. The duration of immobility episodes increased in I-mn-*Sod2* KO mice compared with control animals. i-mn-*Sod2* KO mice displace at a lower speed than controls. Box plots show data distribution and median of the group (black line). The green line inside the boxes indicates the mean. Bonferroni student T-test; *P ≤ 0.05. (For interpretation of the references to color in this figure legend, the reader is referred to the Web version of this article.)

2.4. Absence of neuronal Sod2 increases activation of astrocytes and microglia in the CNS

Increased activation of astrocytes is an indicator of neuroinflammation in neurodegenerative disorders [16]. To test whether neuroinflammation is elevated in neuronal tissues (brain and spinal cord) of i-mn-*Sod2* KO and control mice, the protein expression of GFAP, a marker for astroglial cells, was measured by western blotting. In the spinal cord of i-mn-*Sod2* KO mice, GFAP protein expression was significantly increased (65%) compared to control mice (Fig. 4A). Similarly, GFAP expression was significantly increased (~50%) in the sciatic nerve of i-mn-*Sod2* KO mice relative to control mice (Fig. 4B). Immunofluorescent staining of spinal cord sections with GFAP indicated that the number of astrocytes, in particular activated astrocytes, is increased in i-mn-*Sod2* KO mice (Fig. 4C). Increased expression of GFAP in astrocytes is a marker of activated astrocytes [17]. In addition, we also observed that protein levels GFAP were elevated in the brain of i-mn-*Sod2* KO mice compared to control mice (Fig. S4 A) and an increased number of GFAP positive cells is localized exclusively in hippocampal region of i-mn-*Sod2* KO mice (Fig. S4B).

In addition, we found an increase in activated microglia in the i-mn-*Sod2* KO mice. Immunostaining of spinal cord sections with the microglial marker Iba1 showed an increase in the number of activated microglia in i-mn-*Sod2* KO mice compared to control (Fig. 4D). Similarly, immunofluorescence analysis of spinal cord sections of i-mn-*Sod2* KO mice exhibited increased F4/80 positive staining, a marker for microglial cells or macrophages [18,19] (Fig. 4E).

2.5. Absence of neuronal Sod2 increases inflammatory cytokine expression in the CNS of i-mn-Sod2 KO mice

Microglial and astroglial activation is indicative of an inflammatory response in the CNS. To verify if i-mn-*Sod2* KO mice has increased neuroinflammation, we compared the protein levels of cytokines and chemokines in the spinal cord of i-mn-*Sod2* KO mice and control mice. Of the 40 different cytokines tested in the array of chemokines and inflammatory cytokines, the following showed a significant increase (fold change) in i-mn-*Sod2* KO mice compared to control mice: BLC (2.3); G-CMCF (1.9); IL1-β [2]; IL-1 RA (2.9); IL-6 (2.9); IL-16 (1.6); IL-27 (1.4); JE(1.76); MIP1-alpha (2.2); TARC (3.5) and TIMP1 (3.4) (Fig. 4F and G). These data confirm that there is a heightened inflammatory response in the CNS of the i-mn-*Sod2* KO mice.

2.6. Absence of Sod2 in neurons disrupts blood brain barrier (BBB)

We next analyzed BBB disruption using MRI in i-mn-*Sod2* KO mice 5 months after tamoxifen injection. BBB disruption in different regions of spinal cord and brain was assessed by measuring the increase in MRI intensity due to the accumulation of MRI contrasting agent, Gd-DTPA. The apparent diffusion coefficient (1.5-fold) which represents blood brain disruption and the percentage intensity of Gd-DTPA (~15-fold) were significantly increased in the spinal cord of i-mn-*Sod2* KO mice compared to control mice (Fig. 7A and B). In the brain, a significant increase in permeability was observed in the brain stem (3-fold) and hippocampus (5-fold), but not in the cerebral cortex (Fig. 7C), suggesting that absence of *Sod2* in neurons causes BBB disruption.

2.7. Absence of neuronal Sod2 increases neutrophil infiltration in the spinal cord of mice

Disruption of the BBB can cause infiltration of hematopoietic immune cells in the CNS. Therefore, we compared the infiltration of T cells, B cells, macrophages and neutrophils into the spinal cord and brains of the i-mn-*Sod2* KO mice with control mice. In spinal cords of mice five months after tamoxifen injection, we found no difference in the infiltration of $CD4^{+}$T cells (Fig. 6A). However, the B cells percentage in the spinal cord was elevated (the difference was close to significance, p = 0.07) in the i-mn-*Sod2* KO mice compared to the controls (Fig. 6B). The percentage of macrophages was also similar in the spinal cord of i-mn-Sod2KO compared to control mice (Fig. 6C). We did observe a significant increase in neutrophils (>3 fold) in the spinal cord of the i-mn-*Sod2* KO mice (Fig. 6D). No difference was found in any infiltrating cell type in the brain of i-mn-*Sod2* KO mice compared to control mice (Fig. S4).

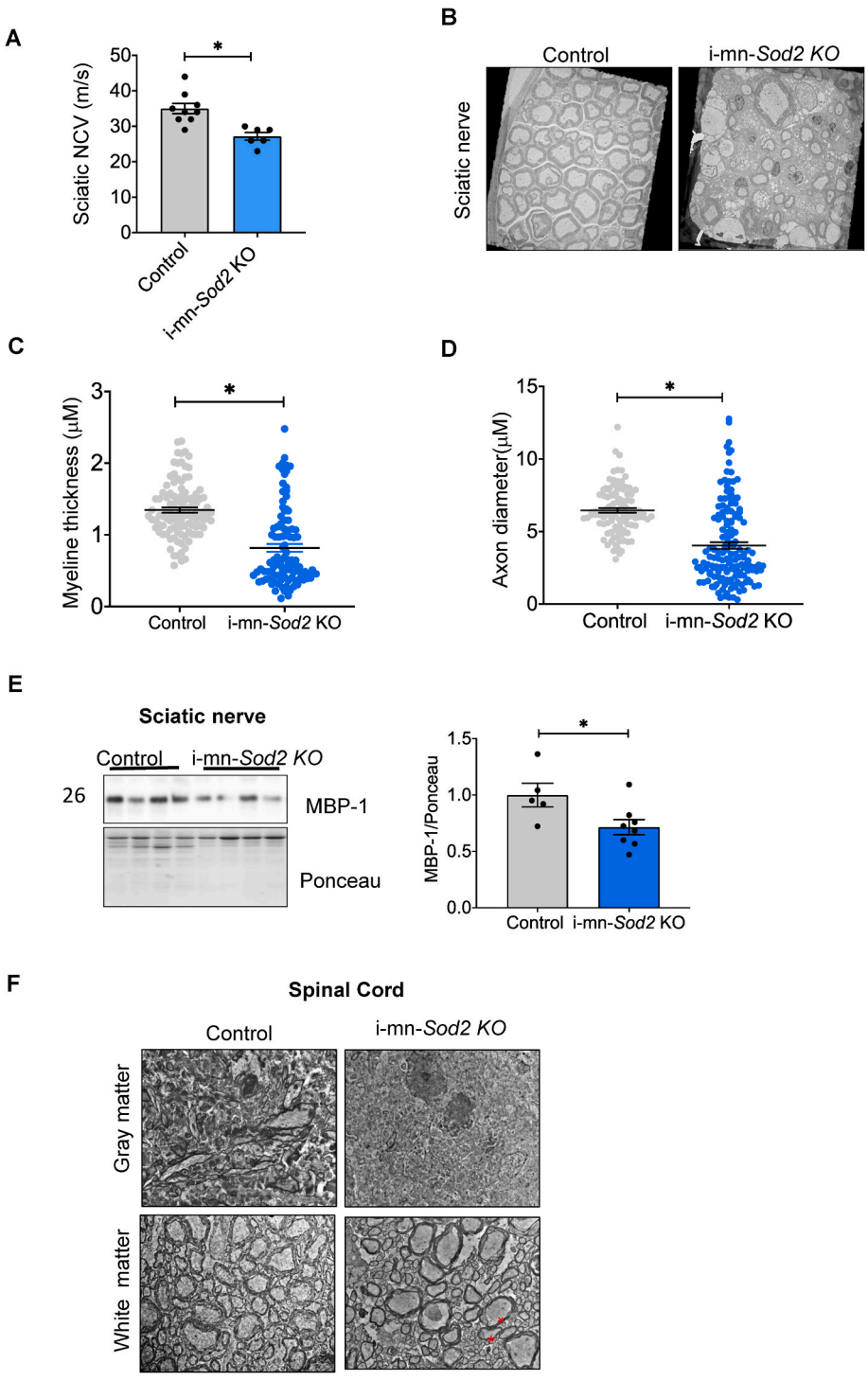

Fig. 3. Deletion of *Sod2* in neurons results in demyelination in sciatic nerve and spinal cord and reduced nerve conduction velocity in i-mn-*Sod2* KO mice. A. Nerve conduction velocity was measured in the sciatic nerve of control (grey bar) and i-mn-*Sod2* KO (blue bar) mice at 7-months of age (n = 6-7group). Data expressed as average ± SEM, student T-test; *P ≤ 0.05. **B.** Electron micrograph of sciatic nerve from control and i-mn-*Sod2* KO mice showing increased demyelination in i-mn-*Sod2* KO mice. Quantification of myelin thickness (**C**) and axonal diameter (**D**) in control and i-mn-*Sod2* KO mice (n = 4). Student T-test; *P ≤ 0.05. **E.** Representative Western blot of MBP expression in sciatic nerve tissue (left panel) and graphical representation of quantified blots, normalized to ponceau stain (right panel). Students unpaired *t*-test, **P* ≤ 0.05. **F.** Representative electron micrograph of spinal cord sections: * shows the sclerosis in white matter. (For interpretation of the references to color in this figure legend, the reader is referred to the Web version of this article.)

2.8. Increased demyelination and decreased nerve conduction velocity (NCV) in i-mn-Sod2 KO mice

The changes in motor coordination and onset of paralysis in i-mn-*Sod2* KO mice led us to ask whether there were changes in sciatic nerve conduction velocity (NCV). We found a significant decrease (~10%) in sciatic nerve conduction velocity (NCV) in i-mn-*Sod2* KO mice compared to control mice (Fig. 3A) consistent with axonal loss and/or demyelination. To further examine these changes, we analyzed electron microscopic images of sciatic nerve sections. The sections from control mice exhibited morphologically normal axons and myelin sheath around the sciatic nerve axons. In contrast, the sciatic nerve of i-mn-*Sod2* KO mice show demyelination and axonal degeneration (Fig. 3B). Quantification of myelin thickness and axonal diameter revealed that both parameters are significantly lower in i-mn-*Sod2* KO mice, compared to control mice (Fig. 3C–D). The level of myelin basic protein (MBP), a major protein component of the myelin sheath in sciatic nerve protein extract was significantly reduced (Fig. 3E). Studies have shown that demyelination in spinal cord is associated with paralysis [18]. Consistent with this, we measured spinal cord sections using electron microscopy and found increased demyelination in white matter and grey matter of i-mn-*Sod2* KO mice (Fig. 3F).

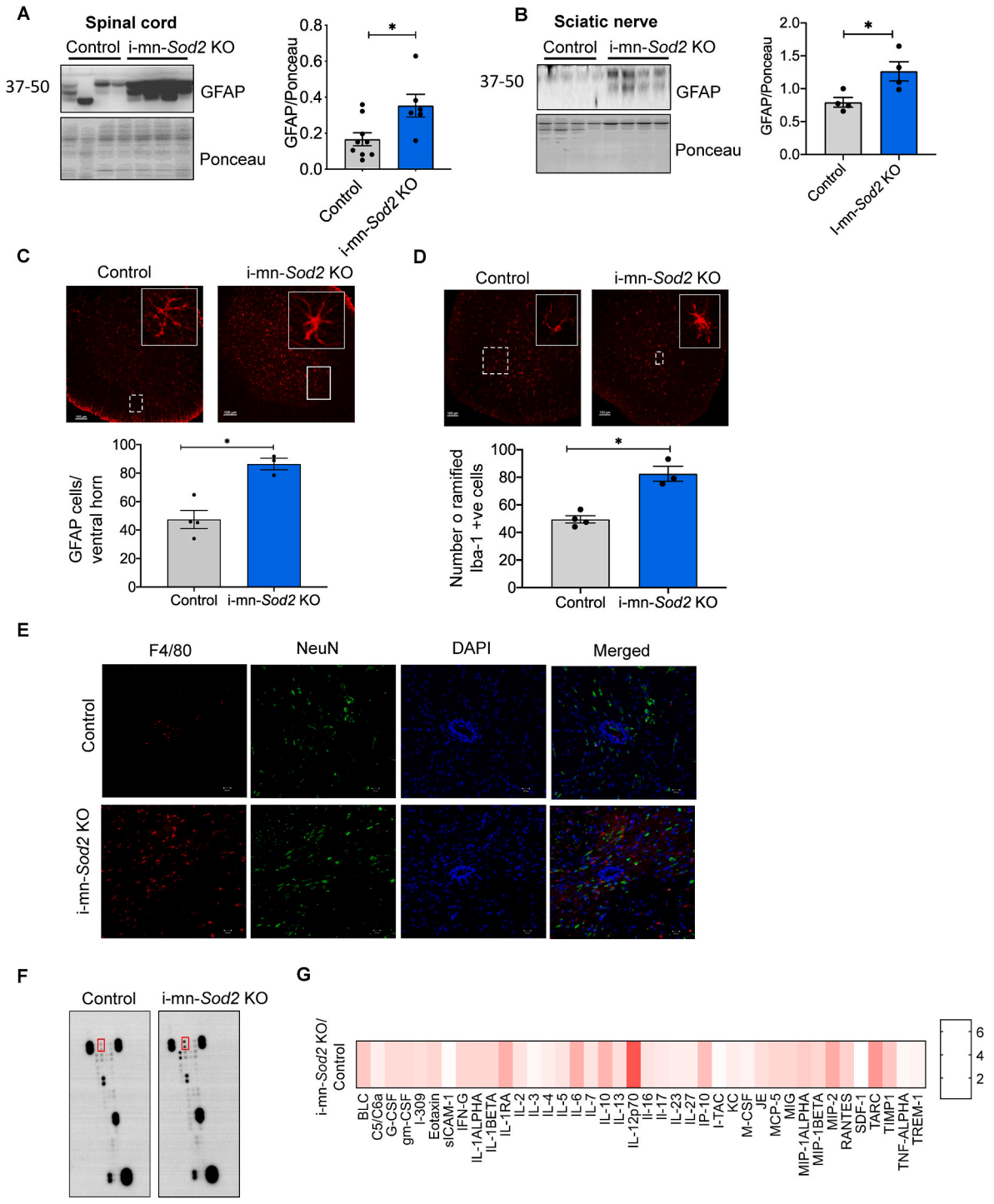

Fig. 4. The inflammatory profile in spinal cord of i i-mn-*Sod2* KO mice is altered.
Representative western blots (left panel) and graphical representation of quantified blots normalized to ponceau (right panel) are shown for GFAP in spinal cord (**A**) and sciatic nerve (**B**) in control (grey bar) and i-mn-*Sod2* KO mice (blue bar). **C**. Representative images of GFAP immune fluorescence in ventral horn of spinal cord of control and i-mn-*Sod2* KO mice (top panel) and quantification of GFAP positive cells (bottom panel) n = 4 mice/group. **D.** Representative images of microglia (Iba-1 positive) (top panel), and quantification of Iba-1 positive microglial cells in lumbar region of spinal cord (bottom panel) n = 4 mice/group. **E**. Immunofluorescence staining of spinal cord sections from control (top panel) and i-mn-*Sod2* KO mice (bottom panel) using antibodies for F4/80 (red) and NeuN (green), DAPI (blue). Merged images of F4/80, NeuN, and DAPI are shown in the far-right column. **F**. Representative image of cytokine blots incubated with spinal cord extract. **G**. Heatmap showing the quantification of inflammatory cytokines/chemokines in spinal cord of i-mn-*Sod2* KO mice, normalized to control mice. Representative image of cytokine profile age 8 months (n = 4). Bonferroni-corrected; *$P \leq 0.05$. . (For interpretation of the references to color in this figure legend, the reader is referred to the Web version of this article.)

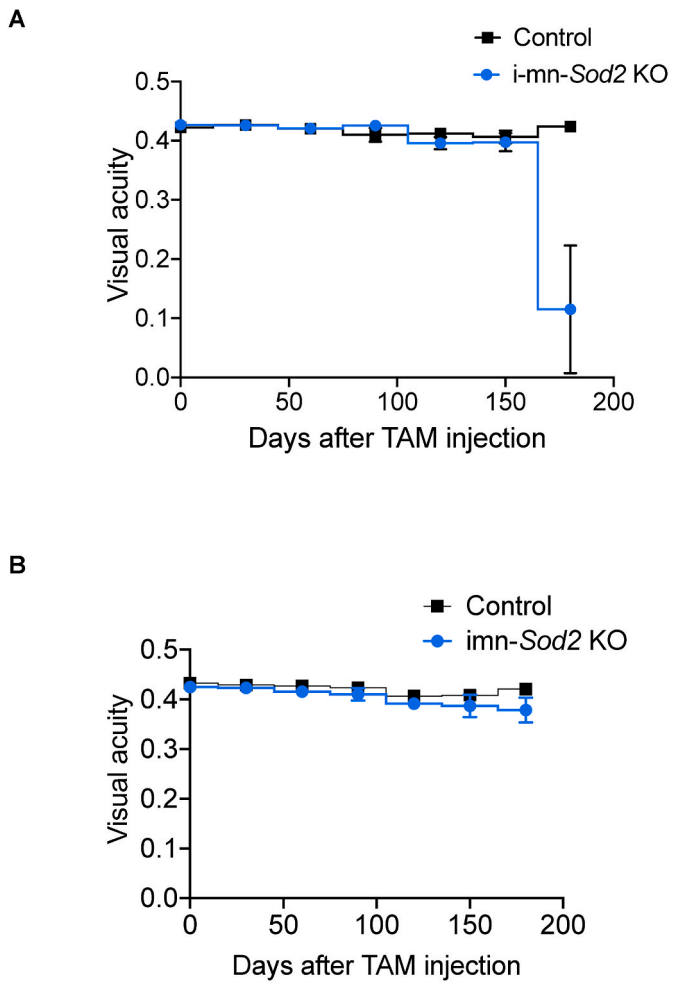

Fig. 5. Visual acuity is reduced in i-mn-*Sod2* KO mice.
Representative time course of acute, monocular episodes of deficits in visual acuity as measured with optokinetic tracking (OKT). Monthly mean acuity in more affected (**A**) or less affected (**B**) eyes of i-mn-*Sod2* KO mice compared to its control animals. Error bars are standard error mean (SEM) n = 4/group.

2.9. Mitochondrial effects of neuron specific deletion of the Sod2 gene

Mitochondrial dysfunction and oxidative stress are associated with many neurological diseases [20]. Therefore, we wanted to determine whether neuronal deletion of the *Sod2* gene would increase mitochondrial generation of reactive oxygen species, altering mitochondrial function and eventually impacting neuronal structure and function. We assessed mitochondrial respiration and hydrogen peroxide production using permeabilized spinal cord. No significant difference in maximal respiration was observed between i-mn-*Sod2* KO and control mice (Fig. 8A). However, mitochondrial hydrogen peroxide generation was significantly elevated during complex I-stimulated respiration (2-fold) and following antimycin A administration (Fig. 8B). Further, there was a trend for hydroperoxide generation to be elevated following the administration of rotenone ($p = 0.08$, Fig. 8B). Western blot analysis of i-mn-*Sod2* KO spinal cord protein extracts showed a significant increase in the levels of mitochondrial complex I (101%), complex-III (22%), complex-IV (91%), however, there is no change in complex V protein content relative to control mice (Fig. 8C). Similarly, mitochondrial outer membrane proteins, TOM20 (5.3-fold) and VDAC (6.2-fold) were significantly increased in i-mn-*Sod2* KO mice (Fig. 8C). To determine whether increased mitochondrial complex protein is associated with increased mitochondrial number, we analyzed mitochondrial number using electron microscopy of spinal cord sections. The number of mitochondria was significantly increased in grey matter (1.4-fold) and white matter (1.4 fold) of 8-month-old i-mn-*Sod2* KO mice relative to control mice (Fig. 8D). Mitophagy is one of the mechanisms that removes the dysfunctional mitochondria, and PINK and PARKIN are the two major proteins involved in mitochondrial quality control. Therefore, we assessed expression levels of PINK and PARKIN in spinal cord protein extracts. Western blot analysis of i-mn-*Sod2* KO spinal cord protein extract showed a significant reduction of PINK1 protein expression (51%), whereas no change in the expression of parkin was observed, relative to control mice (Fig. 8E). We also analyzed the expression of LC3 and P62, two markers of autophagy in the spinal cord extracts. LC3 protein levels in the spinal cord of i-min-*Sod2* KO mice were similar to control mice, whereas p62 expression was increased in imn-*Sod2* KO mice, however, this approach did not reach statistical significance ($p = 0.057$).

2.10. Absence of Sod2 in motor neurons increases the markers of necroptosis in spinal cord

Because the i-mn-*Sod2* KO mice exhibited axonal degeneration and increased inflammation, we asked whether necroptosis, a cell death pathway that causes inflammation [21], was activated in i-mn-*Sod2* KO mice. Phospho-MLKL(p-MLKL) is a biomarker of necroptosis and was found to be significantly increased in the spinal cord (1.7-fold) and sciatic nerve (1.5-fold) of i-mn-*Sod2* KO mice, compared to control mice (Fig. 9A and B, respectively). Similarly, protein expression of MLKL was significantly increased in the spinal cord (1.7-fold) and sciatic nerve (1.5-fold) of i-mn-*Sod2* KO mice relative to control mice ((Fig. 9A and B, respectively).). Expression of NLRP3 inflammasome, a downstream target of necroptosis was also significantly elevated in the spinal cord (1.6-fold) and sciatic nerve (1.6-fold) of i-mn-*Sod2* KO mice relative to control mice (Fig. 9A and B, respectively). Immunofluorescent analysis of spinal cord sections confirmed the increased expression of phospho-MLKL and indicated that phospho-MLKL co-localized with the neuronal marker, NeuN (Fig. 9C). Thus, increased necroptosis might contribute to axonal degeneration and increased inflammation in i-mn-*Sod2* KO mice.

3. Discussion

A growing body of evidence suggests that mitochondrial dysfunction and elevated oxidative stress in neurons are key factors in neurodegenerative diseases such as Alzheimer's disease, Parkinson's disease, and MS [20,22,23]. In support of this, we report here that tamoxifen induced deletion of the mitochondrial antioxidant enzyme MnSOD in post-mitotic neurons leads to a progressive neurological pathology which manifests as gait disturbance, hindlimb paralysis, visual deficits, increased inflammation in neuronal tissues, axonal degeneration, and disruption of blood brain barrier. Previously we reported that neuronal deletion of CuZn-superoxide dismutase (*Sod1)*, a cytosolic antioxidant enzyme, resulted in hindlimb muscle atrophy, NMJ disruption, motor neuron number reduction, and hind limb clasping in old mice [24–26]. Surprisingly, despite the numerous degenerative phenotypes we measured in the i-mn-*Sod2* KO mice, we found no effect on muscle weight, muscle function, motor neuron number, or neuromuscular junction morphology in response to deletion of *Sod2* in neurons.

The neurological signs of i-mn-*Sod2* KO mice are similar to the disease phenotypes observed in the EAE model of MS. These include tail atony, gait abnormality, hind limb clasping, paralysis, and decreased visual acuity [27]. However, there are important differences in EAE mice compared to the i-mn-*Sod2* KO mice. The first difference is timeframe. In EAE, disease signs manifest within two weeks after induction of disease and reach full paralysis by week three. In the i-mn-*Sod2* KO, neurological deficits manifest two months after induction of deletion of *Sod2* and mice eventually develop hindlimb paralysis by five months post deletion. We found that innate immune cells, notability

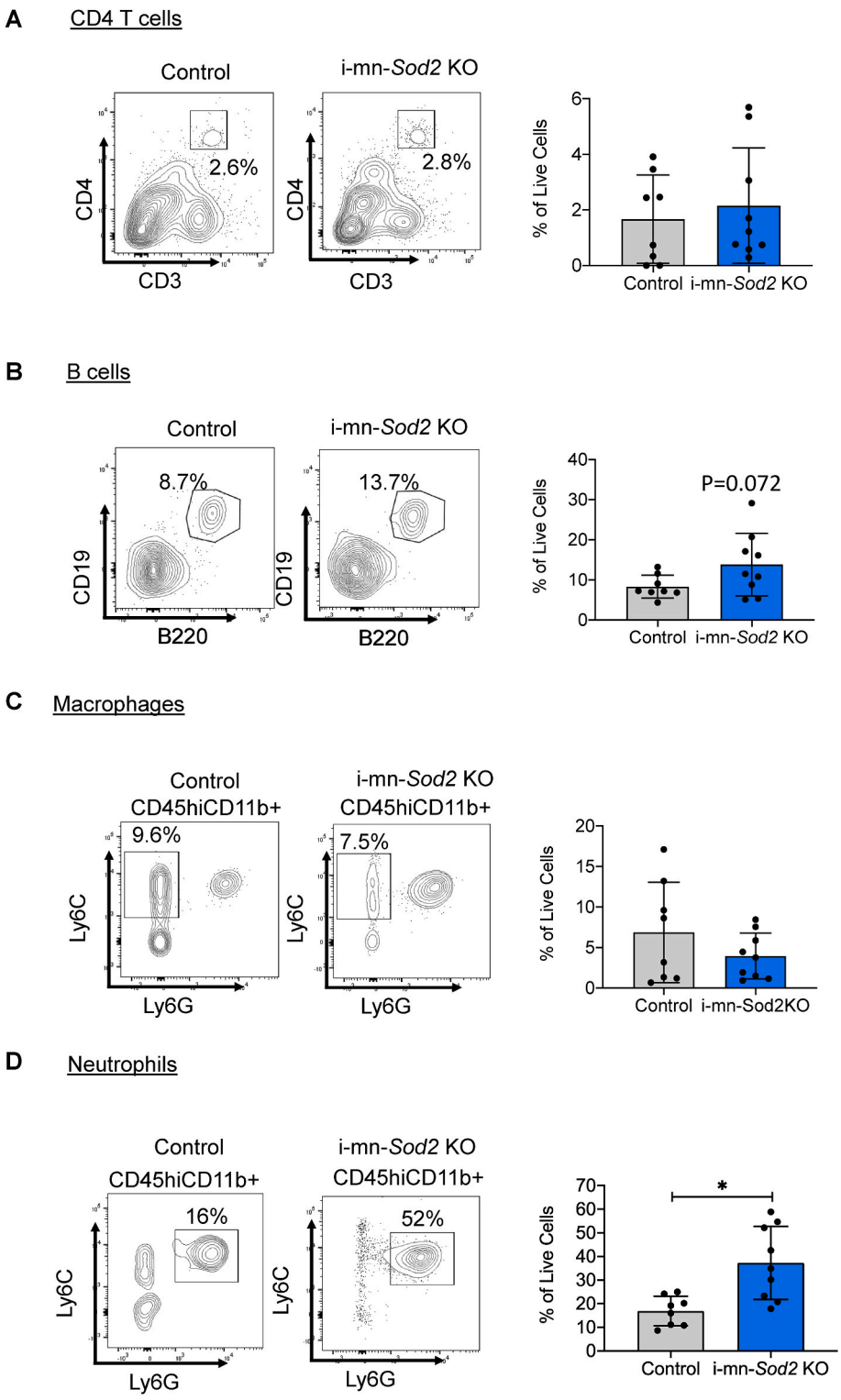

Fig. 6. Deletion of *Sod2* leads to increased infiltration of neutrophils in spinal cord.
Representative flow cytometry plots and percentage of live cells from control (grey bar) and i-mn-*Sod2* KO (blue bar) mice spinal cord for $CD3^{+}CD4^{+}$ T cells (*left*) and quantification (*right*) (**A**); $CD19^{+}B220^{+}$ B cells (*left*) and quantification(*right*) (**B**); Ly6C and Ly6G gating on $CD45^{hi}CD11b^{+}$ cells for macrophages ($CD45^{hi}CD11b^{+}Ly6C^{+}Ly6G^{low}$) (*left*) and quantification (*right*) (**C**); Ly6C and Ly6G gating on $CD45^{hi}CD11b^{+}$ cells for neutrophils ($CD45^{hi}CD11b^{+}Ly6C^{+}Ly6G^{+}$) (*left*) and quantification (*right*) (**D**). (n = 5/group). Error bars represent SEM and Student *t*-test was used to determine statistical significance (*p < 0.05). . (For interpretation of the references to color in this figure legend, the reader is referred to the Web version of this article.)

neutrophils, had infiltrated in spinal cord of imn-*Sod2* KO mice. Neutrophils are involved in the driving pathology in EAE models and high neutrophil signatures have been associated with progressive versions of MS. The i-mn-Sod2 KO mice may also have a deletion in *Sod2* in T cells as the Slick H Cre controlled by the Thy1 promoter may also be expressed in immune cells. We found that the i-mn-*Sod2* KO mice had similar numbers of T cells the CNS compared to control mice. This suggests that T cells are not a major cell type contributing to the neuropathology in these mice. Interestingly, our data shows that peripheral nerves, specifically the sciatic nerves, are also affected in the i-mn-*Sod2* KO mice. Historically, peripheral neuropathies were not associated with MS disease. However, newer magnetic resonance neurography techniques show that peripheral nerves are dysfunctional in MS and may be a result of demyelinated [28,29]. The i-mn-*Sod2* KO may provide opportunities to study MS disease states with both central and peripheral demyelination.

Mitochondrial dysfunction is a key feature of aging and neurodegenerative diseases and is proposed to play an important role in all

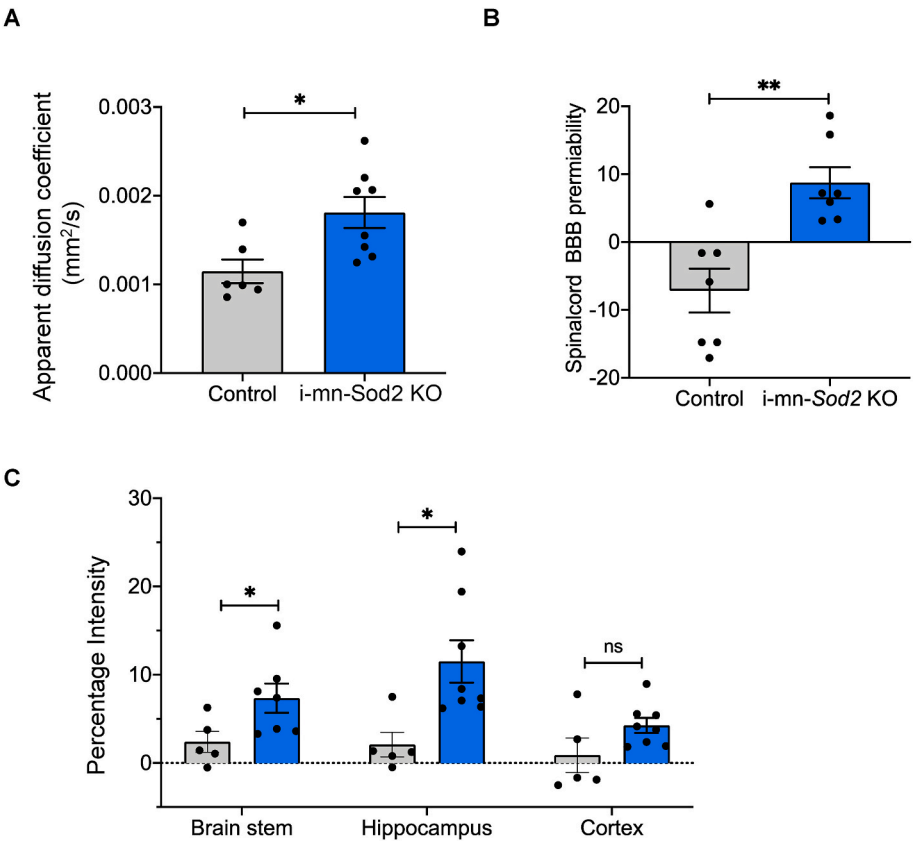

Fig. 7. Neuronal deletion of *Sod2* disrupts blood brain barrier and CNS inflammation.
MRI data showing apparent diffusion coefficient (**A**), BBB disruption in spinal cord (**B**), and different regions of brain (**C**). Bars represent mean ± SEM (n = 7–8 per group) and are expressed relative to wild type control. Students unpaired *t*-test, $^{*}P \leq 0.05$. Control (grey bar) and i-mn-*Sod2* KO (blue bar). . (For interpretation of the references to color in this figure legend, the reader is referred to the Web version of this article.)

stages of MS in patients as well as in animal models [30–36]. In our study, we found that mitochondrial number and oxidative stress are increased in the spinal cord of i-mn-*Sod2* KO mice. Interestingly, increased axonal mitochondrial content and mitochondrial complex protein IV activity are observed in demyelinated axons in MS patients [37–40]. Similarly, increased mitochondrial content, altered mitochondrial morphology, and mitochondrial dysfunction are also reported in EAE mouse model [41–43]. The increase in mitochondrial number has been proposed to be an adaptive change to restore function in demyelinated axons (*38*). Previously, we found that deletion of *Sod2* in skeletal muscle also resulted in increased mitochondrial content and oxidative stress [44] and adipocyte specific deletion of *Sod2* is reported to increase mitochondrial content in adipose tissue [45]. This suggests that irrespective of the nature of the tissue, *Sod2* deletion can increase mitochondrial content and could be an adaptive change in response to the deficiency of a critical antioxidant enzyme in the mitochondria.

Like mitochondrial dysfunction, oxidative stress has been implicated in neurodegenerative diseases such as Alzheimer's disease and Parkinson's disease [20,46] and has also been tied to the pathogenesis of MS [47,48]. One of the pathways induced by oxidative stress is necroptosis, a form of programmed cell death that causes inflammation [49]. Necroptosis is activated in the brains of MS patients as well as in mouse models of MS [50]. Pharmacological or genetic inhibition of necroptosis protected against demyelination, reduced inflammation, and oligodendrocyte degeneration in MS mouse models, supporting a role of necroptosis in MS pathogenesis [51]. In addition to MS, necroptosis is reported to be elevated in several neurodegenerative diseases such Alzheimer's disease, Parkinson's disease, and in amyotrophic lateral sclerosis (ALS) [52] In our study, we observed an increase in necroptosis markers in the neurons of i-mn-*Sod2* KO mice in the absence of neuronal loss. Axonal degeneration is a major cause of permanent neurological damage during multiple sclerosis [53] and recent studies identified necroptosis as a key mechanism for axonal degeneration [53–55]. Importantly, pharmacological inhibition of necroptosis delayed axonal degeneration in the peripheral nervous system and CNS [54]. Inhibiting necroptosis reduced neuroinflammation in neurodegenerative diseases including MS [51,56] supporting a role of necroptosis in neuroinflammation. Leucine rich repeat containing protein family, pyrin domain containing 3 (NLRP3) is a key modulator of inflammation that can be activated by necroptosis. NLRP3 expression is increased in EAE mouse model of MS, and the severity disease was reduced in *Nlrp3* knock out mice, supporting a role of inflammation in MS pathogenesis [57]. Recently it was reported that NLRP3 can be used as an indicator for progressive versions of MS [58,59] and in our study protein expression of NLRP3 was strongly upregulated in i-mn-*Sod2* KO mice, supporting a role of NLRP3 in inflammation.

Inflammation is characterized by increased production of proinflammatory cytokines and chemokines. In our mouse model, we observed an increase in the expression of several proinflammatory cytokines and chemokines such as granulocyte colony stimulating factor (GM-CSF), IL1-beta, IL1-RA, IL-6, IL-27, JE/MCP1, and IP-10. A similar cytokine and chemokine panel was also reported in MS patients and mouse models of MS [60,61]. Interestingly, CXCL13 (BLC), a chemokine involved in the migration of B cells is elevated in demyelinating axons of MS patients [62,63] and in our study increase in CXCL13 correlates with the elevated levels of infiltrating B-cells in the spinal cord [64]. BBB disruption is also a proposed mediator of inflammation in the CNS [65] and a significant increase in BBB disruption in the spinal cord of i-mn-*Sod2* KO mice was detected. Thus, increased inflammation in the spinal cord of i-mn-*Sod2* KO mice could be multifactorial: increased oxidative stress, necroptosis and NLRP3 activation, and BBB disruption.

In i-mn-*Sod2* KO mice, we observed axonal degeneration as indicated by reduced myelin thickness and loss of nerve conduction velocity. Similar observations are reported in MS patients and mouse models of MS and inflammation is reported to be the major cause for axonal degeneration in MS [34]. Recent evidence suggests that dysfunctional

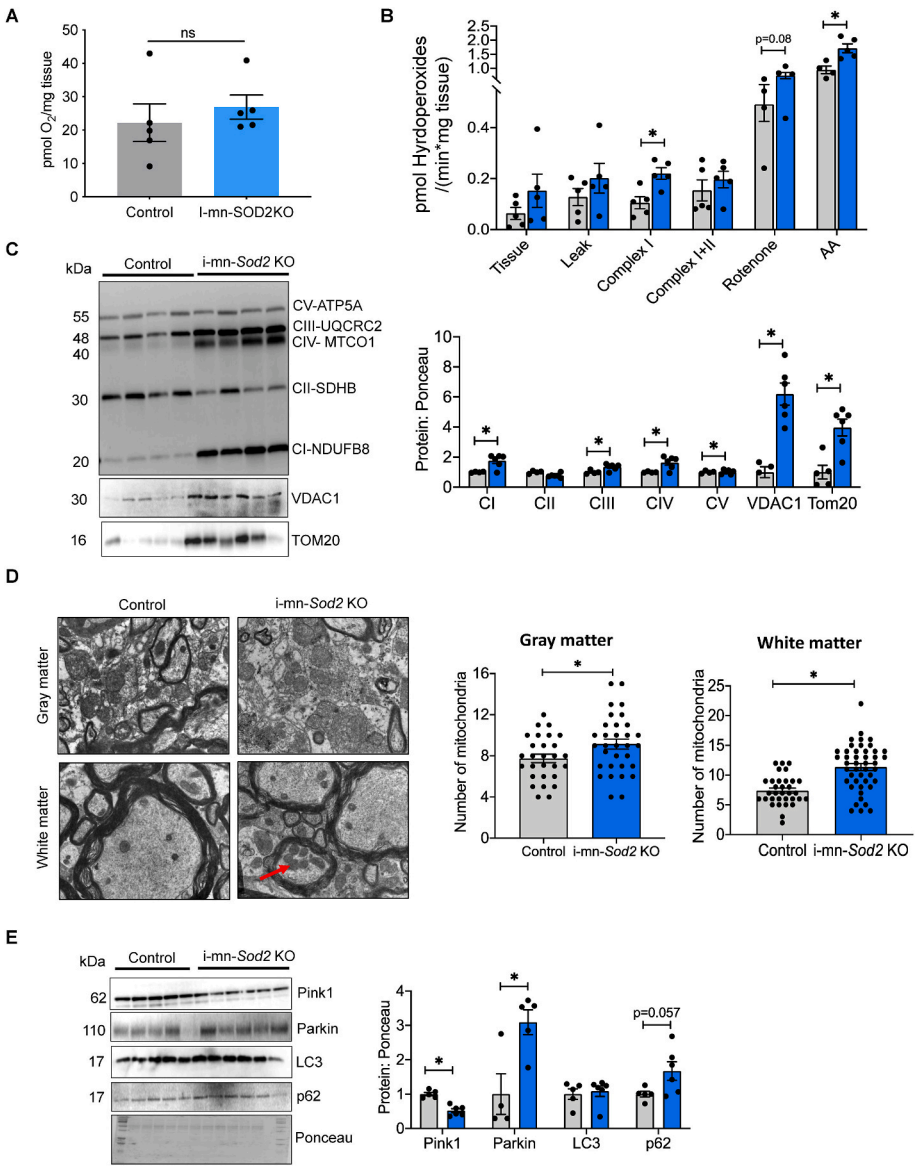

Fig. 8. Reduction of *Sod2* in neurons alters mitochondrial peroxide generation, mitochondrial morphology and expression of proteins involved in mitophagy

A. Basal respiration in spinal cord of control and i-mn *Sod2* KO mice measured 5 months post tamoxifen injection. **B.** H_2O_2 production in spinal cord in the presence of different substrates/inhibitors for mitochondrial complexes added sequentially. Leak state: Glutamate (10 mM) and malate (2 mM) with absence of ADP; Complex I: 2.5 mM ADP in addition of the leak state; Complex I + II Succinate (10 mM); Complex II: 0,5 μM rotenone and Complex IV addition of antimycin (AA) measurements normalized to spinal cord wet weight. **C.** Western blot of spinal extracts for mitochondrial proteins (left panel) and quantification of mitochondrial proteins normalized to ponceau. **D.** TEM representative images of spinal cord cross section (left panel). Quantification of number of mitochondria in grey matter and white matter (right panel). **E.** Western blot of spinal extracts for protein involved in mitophagy and autophagy (left panel). Quantification is shown in the right panel. Control (grey bar) and i-mn-*Sod2* KO (blue bar). . (For interpretation of the references to color in this figure legend, the reader is referred to the Web version of this article.)

mitochondria are also involved in axonal degeneration [66]. In mouse models of MS, increased necroptosis of oligodendrocytes is attributed to the demyelination process. Whether oligodendrocytes undergo necroptosis in of i-mn-*Sod2* KO mice remains to be tested.

Patients with multiple sclerosis can be categorized as relapsing-remitting or progressive. Relapsing-remitting MS patients have T cells infiltration into the CNS causing disability (relapse) which is followed by periods of recovery (remission). Progressive MS patients do not experience relapses and remissions but rather disability gradually progresses in the absence of infiltration of T cells into the CNS [67]. We speculate that the i-mn-*Sod2* KO mice actually model aspects of progressive MS for the following reasons. First, neurological dysfunction develops progressively in the mice which reflects disease course in progressive MS patients. Second, unlike EAE, T cells are not present in the CNS of the i-mn-Sod2 KO mice. Third, the mitochondrial dysfunction and elevation in the NLRP/inflammasome pathways observed in the CNS of i-mn-Sod2 KO mice are prominent molecular features in progressive forms of MS [58]. EAE, on the other hand, may better reflect an acute relapse in MS because disease develops quickly and is driven by auto-reactive T cells. It is unclear if the initiating event of MS disease is due to a dysregulation of the immune system or if the disfunction lies in the cells of the nervous system such as neurons or oligodendrocytes. Recent GWAS studies have identified two polymorphisms in genes highly expressed in neurons that are associated with risk in developing primary progressive MS, KIF5A and REEP1 [68]. REEP1 is of particular interest, as it is involved in the protein folding during at the mitochondria and the endoplasmic reticulum junctions during stress responses [69,70]. These observations suggest that dysfunction in neuronal stress responses is involved in the etiology of progressive MS. Our data with the imn-Sod2 KO mice experimentally shows that dysfunction of the stress response in neurons alone triggers a demyelinating disease that resembles primary progressive MS. Currently, there are no genetically modified animal models to study multiple sclerosis progression. Furthermore, there are currently few therapeutic options for people with progressive MS. Based on our findings, we propose that i-mn-*Sod2* KO mice could be used as a preclinical model of progressive MS. However, further studies need to be performed to assess the use of i-mn-*Sod2* KO mice as a model of MS.

In summary, our data show that a reduction of MnSOD in spinal cord neurons promotes a phenotype of demyelination, inflammation, and progressive paralysis that mimics phenotypes associated with multiple sclerosis but does not induce muscle atrophy and weakness.

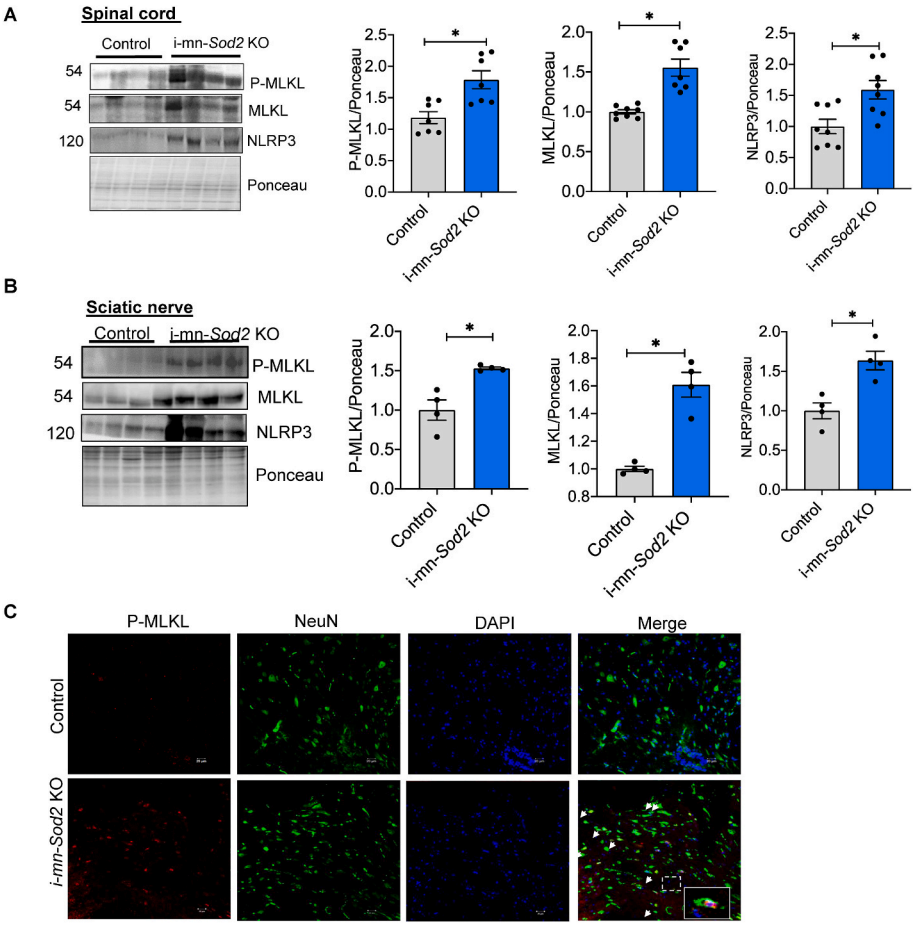

Fig. 9. Markers of necroptosis and inflammation in neuronal tissues from i-mn-*Sod2* KO mice. Representative western blots showing expression of phospho-MLKL, MLKL, and NLRP3 in spinal cord (**A**) and sciatic nerve (**B**) of 8-month-old control (grey bar) and i-mn-*Sod2* KO (blue bar) mice (n = 7–8 per group, mixed male and female). Mice were injected with tamoxifen at 2–3 months of age. **C.** Immunofluorescence staining of spinal cord sections from control (top panel) and i-mn-*Sod2* KO mice (bottom panel) using antibodies for phospho-MLKL (red) and NeuN (green), DAPI (blue). Merged images of phospho-MLKL, NeuN, and DAPI are shown in the far-right column and yellow color represents colocalization of phospho-MLKL and neurons. Bars represent mean ± SEM (n = 7–8 per group) and are expressed relative to control. Students unpaired *t*-test, $^{*}P \leq 0.05$. (For interpretation of the references to color in this figure legend, the reader is referred to the Web version of this article.)

4. Materials and methods

Generation of i-mn-Sod2KO mice. Slick-H transgenic mice that express a CreER^{T2} fusion protein and an enhanced yellow fluorescent protein (EYFP) directed by two separate copies of the modified mouse *Thy1* promoter region were obtained from Jackson Laboratories (Bar Harbor, ME). The expression of SLICK H Cre was previously confirmed in all motor neurons, hippocampal and dorsal root ganglion neurons and in varying degrees in cortex and other neuronal populations [71].To determine the effect of deletion of MnSOD in motor neurons, we generated the i-mn-*Sod2* KO (*Sod2*$^{flox/flox}$; Slick-H Cre^{pos}) mice by breeding *Sod2*$^{flox/flox}$; Slick-H Cre^{pos} males to *Sod2*$^{flox/flox}$; SlickHCre^{neg} females. At 2–3 months of age, male and/or female *Sod2*$^{flox/flox}$; Slick-H Cre^{pos} and *Sod2*$^{flox/flox}$; Slick-H Cre^{neg} (control) mice were given an intraperitoneal injection of tamoxifen (Sigma, St Louis MO) dissolved in corn oil for 5 consecutive days (60 mg/kg body weight). Five months after tamoxifen or corn oil injection, mice were euthanized, and brain, spinal cord, sciatic nerve, and muscle tissues were collected. All animal procedures in this study were approved by Institutional Animal Care and Use Committees of the Oklahoma Medical Research Foundation.

Quantitative magnetic resonance imaging. Fat mass and lean mass of mice was analyzed by quantitative magnetic resonance [EchoMRI (Echo Medical Systems, Houston, TX, USA)] imaging during the light phase as described earlier [72].

Gait assessment by footprint. Hind paws of mice were coated with non-toxic ink and mice were allowed to walk on white paper. Distance between the two paw prints (stride length) were measured [73]. Mean values were used for statistical analysis.

Locomotor activity test. Locomotor activity test: We tested each mouse individually in a Plexiglas chamber (40 cm × 40 cm X 40 cm) during their dark cycle. The spontaneous activity of the animals was video recorded for 30 min and analyzed offline using ANY-Maze video tracking software (Stoelting Co. Wood Dale, IL). Distance traveled in meters (m), immobility episodes in seconds (s) and average speed (m/s) were compared between the two genotypes. We performed Bonferroni student T-tests on the data using SigmaStat 4 software (Systat Software, Inc. San Jose, CA).

Western blot analysis. Western blot analysis was performed as described previously [74]. In brief, tissues were homogenized in homogenization buffer (50 mmol/L HEPES (pH 7.6), 150 mmol/L sodium chloride, 20 mmol/L sodium pyrophosphate, 20 mmol/L β-glycerophosphate, 2 mmol/L EDTA, 1.0% Igepal, 10% glycerol, 2 mmol/L phenylmethylsulfonyl fluoride, and protease inhibitor cocktail) and proteins were quantified using Bradford reagent (Bio-Rad, California, USA). Equal quantity of proteins was separated in SDS-PAGE and proteins were transferred to PVDF membrane. The membrane was blocked with 1% BSA in Tris buffed Saline -Tween (0.1%) followed by overnight incubation with primary antibodies in 1% BSA. The blots were washed and incubated with HRP-conjugated secondary antibody for 1 h, and protein bands were detected by ECL reagent using (G-Box Syngene). The band intensity was quantified by NIH image J. The following primary antibodies were used: Sod1; Sod2, MLKL (Enzo Life science, NY, USA), mitochondria complex protein (ThermoFisher Scientific, USA), NeuN (Cell Signaling technology, Danvers, USA), MBP, GFAP; phospho-MLKL; PINK1 (Abcam, Waltham, USA), GAPDH; β-actin (Sigma Aldrich, St. Louis, USA), NLRP3 (Adipogen Life Sciences, San Diego, USA).

Immunofluorescence. Immunofluorescence was performed as previously described [75]. Briefly, animals were perfused with cold PBS and spinal cord was collected. Lumber region of the spinal cord was fixed in 4% PFA overnight and transferred to 30% sucrose in PBS at 4 °C

overnight. The spinal cord was embedded in O.C.T compound (Sakura Finetek, USA). Embedded tissue was cut into 20 μm transverse sections using a cryostat and mounted on microscopic glass slides (Thermo Fisher Scientific, USA). For immunofluorescence, the sections were incubated in blocking buffer (5% (v/v) normal goat serum (Sigma Aldrich, xx) and 0.2% (v/v) Triton X-100 (Sigma Aldrich) in PBS) for 1 h at room temperature. The sections were incubated with antibodies for neurons (NeuN); microglia (Iba-1) (Wako chemicals, USA), and astrocytes (GFAP- Abcam, Waltham, USA), and phospho-MLKL at 4 °C overnight in a humidified chamber. Images were captured using a confocal microscope (Nikon Instruments Inc, USA) and the number of motor neurons were counted in ventral horn region of spinal cord. Activated microglia and activated astrocytes were counted based on the reactivity of Iba-1 and GFAP antibodies. To quantify the number of GFAP and Iba-1 cells, 5 lumbar sections per mouse were used. The number of GFAP or Iba-1 positive cells from 5 sections per mouse were counted and the average per mouse is represented.

Ultrastructure of sciatic nerve and spinal cord. Sciatic nerve and spinal cord samples were immediately collected after sacrifice and samples were fixed in a 2% paraformaldehyde/2.5% glutaraldehyde mix in 0.1 M sodium phosphate buffer (pH 7.4) for 24 h at 4 °C, then post fixed 1 h in 1% Osmium tetroxide (in the same buffer). Samples were then dehydrated using a modified gradient ethanol/propylene oxide series and embedded in Epon/Araldite resin. The specimens were cut into ultrathin sections and stained with lead citrate and uranyl acetate. The sections were examined under Hitachi H7600 Transmission Electron Microscope at 80 kV. For analysis of myelin thickness and axon diameter, 4 sections/mouse were taken and counted. The pooled data from 16 sections for each group is shown in the figures. Axonal diameter and myelin thickness were measured using ImageJ software.

Nerve Conduction Studies. Nerve conduction velocity (NCV) was measured as we have previously described [76]. All experiments were performed with a Nicolet Viking Quest portable EMG apparatus (Natus Medical Incorporated, USA). Mice were anesthetized with continuous flow of a mixture of oxygen and isoflurane and body temperature was maintained using heating pad. Sciatic NCV was measured by stimulating proximal ankle electrodes with a current (mA) and the latency for response at the dorsal digits divided by the distance traveled was measured. Then the stimulating electrodes were placed at the sciatic notch and the latency to the ankle was measured, subtracted from the initial foot ankle latency, and divided by the notch to the ankle to obtain values for sciatic NCV.

Spinal cord permeabilization for respirometry. In brief, (10 mg) spinal cord was carefully dissected and cut into small pieces in an ice-cold buffer X containing (in mM) 7.23 K_2EGTA, 2.77 CaK_2EGTA, 20 imidazole, 0.5 DTT, 20 taurine, 5.7 ATP, 14.3 PCr, 6.56 $MgCl_2$-$6H_2O$, 50 K-MES, 0.5 glutamate, and 0.2 malate (pH 7.1). The spinal cord pieces were permeabilized in saponin solution (80 μg/mL) for 30 min at 4 °C, followed by washes in ice-cold *buffer Z* containing (in mM) 105 K-MES, 30 KCl, 10 K_2HPO_4, 5 $MgCl_2.6H_2O$, 0.5 mg/ml BSA, and 0.1 EGTA (pH 7.1) for 15 min.

Simultaneous high-resolution respirometry and fluorometry measurements. Oxygen consumption rate (OCR) and the rate of mitochondrial hydrogen peroxide (H_2O_2) production were simultaneously measured using the Oxygraph-2k (O2k, OROBOROS Instruments, Innsbruck, Austria) as described before [77] with minor modifications. OCR was determined using oxygen probe, while rates of H_2O_2 generation was determined using O2k-Fluo LED2-Module Fluorescence-Sensor Green. Measurements were performed on permeabilized fibers in *buffer Z* media at 37 °C containing 10 μM Amplex® UltraRed (Molecular Probes, Eugene, OR), 1 U/mL horseradish peroxidase (HRP), and blebbistatin (25 μM). HRP catalyzes the reaction between H_2O_2 and Amplex UltraRed to produce the fluorescent resorufin (excitation: 565 nm; emission: 600 nM). The fluorescent signal was converted to nanomolar H_2O_2 via a standard curve established on each day of experiments. Background resorufin production was subtracted from each measurement. Rates of respiration and H_2O_2 production were determined using sequential additions of substrates and inhibitors as follows: glutamate (10 mM), malate (2 mM), ADP (2.5 mM), succinate (10 mM), rotenone (0.5 μM) and antimycin A (1 μM). All respiration measurements were normalized to antimycin A to account for non-mitochondrial oxygen consumption. Data for both OCR and rates of H_2O_2 generation were normalized to milligrams of sciatic nerve wet weight.

Contractile measurements. Muscle contractile measurements were performed on isolated extensor digitorum longus (EDL) muscle using a 1200A *in vitro* test system (Aurora Scientific Inc., Aurora, ON, Canada), as previously described [78]. Briefly, the EDL muscles were attached to a model 300C servomotor (Aurora Scientific Inc.) within a water bath containing an oxygenated Krebs-Ringer buffer at 32 °C. A model 701C stimulator (Aurora Scientific Inc.) was used to generate supramaximal voltage at 0.2 ms pulse width for adjusting optimal muscle length for force production. A train of stimuli (300 ms duration, 150 Hz strength) was used to generate data on muscle fatigue, while stimulation frequencies between 1 and 300 Hz were used to generate force frequency curves. Specific force (N/cm2) was adjusted for muscle length and weight, while the data were analyzed using commercial software (DMC and DMA, Aurora Scientific Inc.) [79].

Mouse spinal cord cytokine array analysis. Protein profile array (Mouse Cytokine Array Panel A #ARY006, R&D Systems, Minneapolis, MN) was used to quantify the inflammatory cytokines in spinal cord according to the manufacturer's instructions. Briefly, after perfusing the animals with cold PBS, mouse spinal cord was dissected out and the lumbar region of the spinal cord was homogenized in PBS in the presence of protease inhibitor cocktail. Extracts containing 200 μg of protein were used for the assay.

Flow-cytometry. Infiltrating and resident cells were isolated from the brains and spinal cords of PBS-perfused mice as described (REF). For this, CNS homogenates were incubated with collagenase (Roche diagnostics) and DNAse (Sigma, St Louis MO) for 45 min at 37 °C, purified by a Percoll gradient and washed with PBS. Cells were stained with the following antibodies in various combinations purchased from BioLegend (San Diego, USA): CD45-FITC, CD19-PerCP-Cy5.5, CD3-PE, B220-PECy7, CD11b-APC, Ly-6G-BV711, CD4-BV421 and Ly6C-APC-Cy7. All cells were passed through a LSRII flow cytometer and data were analyzed using FlowJo software (Tree Star Inc, USA**).**

Visual acuity assessment. Visual acuity onset was analyzed monthly by the optokinetic tracking (OKT) response using Optometry software and apparatus (Cerebral Mechanics Inc., Alberta, Canada) as previously described [15]. Briefly, freely moving mice were placed on a platform, which is surrounded by a virtual cylinder rotating at varying frequencies. Visual acuity is represented as the highest spatial frequency at which mice track the rotating cylinder. Optokinetic tracking is a temporal-to-nasal reflex, with counter-clockwise and clockwise rotations exclusively testing the right and left eye, respectively.

Mouse magnetic resonance imaging (MRI). Five months after the initial tamoxifen injections to induce genetic deletion of *Sod2* in neurons, I-mn-*Sod2* KO (n = 7–8) and wild type (n = 5) mice were used for MRI experiments using a Bruker Biospec 7.0 T/30 cm horizontal-bore imaging spectrometer. Experiments were carried out under general anesthesia (1–2% Isoflurane, 0.8–1.0 L/min O_2) and mice were restrained. After, injecting a bolus of 0.4 mg/kg of gadolinium through tail vein, mice were placed in an MR-compatible cradle and inserted in a MR probe. Spinal cord and brain were localized by MRI and imaged using a Bruker S116 gradient coil (2.0 mT/m/A) and a 72 mm quadrature multi-rung RF coil [21] In-vivo diagnostic contrast-enhanced MRI approach with injection of gadolinium contrast via an intravenous tail-vein catheter was performed at 10 min post-contrast to assess for an intact BBB. This assessment used multi-slice spin echo T1-weighted images (TR = 1000.0 ms, TE = 14 ms, FOV = 2.50 × 2.50 cm2, averages = 2, slices = 16, matrix size = 256 × 256) attained before and 15 min after tail vein gadolinium contrast agent injection (Gd-DTPA, Magnevist, Bayer Inc., Wayne, NY, USA; 0.4 mmol/kg) (Thomas et al.,

2020). Diffusion-weighted imaging (DWI) was also used to characterize the mobility of water in brain tissue. A coronal axial multi-slice DWI sequence covering the entire brain was performed with the following parameters: TR = 3000 ms, TE = 32.5 ms, matrix size = 96 × 96, slice thickness = 0.75 mm. Apparent diffusion coefficient (ADC) values were acquired by placing four circular regions-of-interest (ROIs) within various brain and spinal cord regions, with values averaged [80].

Statistical analysis: Results are expressed a means of ±S.EM. Statical analysis was performed in GraphPad Prism 9.0 software. Bonferroni corrections were used for cytokine array analysis. Student's *t*-test was used to compare to between the groups.

Author contributions

Conceptualization: SB; RCA, HVR, Methodology: SB, GK, RCV, SSD, TN, SM, AM, JB, KP, SD, DW, NS, DS, Investigation: SB, RCA, HVR, Supervision: HVR and RCA, Writing original draft: SB, HVR, Writing -Review and editing: RCA, HVR, TLL, SF, SSD, AR.

Data and materials availability

All data required to evaluate the conclusions in the paper are present in paper and the supplementary materials.

Funding

This work was supported by NIA-AG051442, NIA AG050676, VA Merit I01BX004453 and VA Senior Career Scientist award IK6BX005234 to HVR as well as a grant to RCA and HVR from the Presbyterian Health Foundation, USA. RCA is also supported by NIH 1RO1 AI 131624-01A1. Further support includes a VA Senior Career Research Award (1IK6BX005238) and VA Merit I01BX004538 to AR, R01 AG052606 and Oklahoma Center for Adult Stem Cell Research, a program of Oklahoma Tobacco Settlement Endowment Trust (TSET) to MJB, NIH R01 AG059718 to SSD, and support from NIH (NIMGS R35GM137921) and the Presbyterian Health Foundation, USA to TLL.

Declaration of competing interest

The authors declare that they have no competing interests.

Data availability

Data will be made available on request.

Appendix A. Supplementary data

Supplementary data to this article can be found online at https://doi.org/10.1016/j.redox.2022.102550.

References

[1] E. Tonnies, E. Trushina, Oxidative stress, synaptic dysfunction, and Alzheimer's disease, J Alzheimers Dis 57 (2017) 1105–1121.
[2] J. Blesa, I. Trigo-Damas, A. Quiroga-Varela, V.R. Jackson-Lewis, Oxidative stress and Parkinson's disease, Front. Neuroanat. 9 (2015) 91.
[3] K. Ohl, K. Tenbrock, M. Kipp, Oxidative stress in multiple sclerosis: central and peripheral mode of action, Exp. Neurol. 277 (2016) 58–67.
[4] P. Wang, K. Xie, C. Wang, J. Bi, Oxidative stress induced by lipid peroxidation is related with inflammation of demyelination and neurodegeneration in multiple sclerosis, Eur. Neurol. 72 (2014) 249–254.
[5] S.C.W. Ng, R. Furman, P.H. Axelsen, M.S. Shchepinov, Free radical chain reactions and polyunsaturated fatty acids in brain lipids, ACS Omega 7 (2022) 25337–25345.
[6] Y. Li, et al., Dilated cardiomyopathy and neonatal lethality in mutant mice lacking manganese superoxide dismutase, Nat. Genet. 11 (1995) 376–381.
[7] R.M. Lebovitz, et al., Neurodegeneration, myocardial injury, and perinatal death in mitochondrial superoxide dismutase-deficient mice, Proc. Natl. Acad. Sci. U. S. A. 93 (1996) 9782–9787.
[8] S. Lynn, et al., Selective neuronal vulnerability and inadequate stress response in superoxide dismutase mutant mice, Free Radic. Biol. Med. 38 (2005) 817–828.
[9] T. Ikegami, et al., Model mice for tissue-specific deletion of the manganese superoxide dismutase (MnSOD) gene, Biochem. Biophys. Res. Commun. 296 (2002) 729–736.
[10] V. Heimer-McGinn, P. Young, Efficient inducible Pan-neuronal cre-mediated recombination in SLICK-H transgenic mice, Genesis 49 (2011) 942–949.
[11] E. Takahashi, K. Niimi, C. Itakura, Motor coordination impairment in aged heterozygous rolling Nagoya, Cav2.1 mutant mice, Brain Res. 1279 (2009) 50–57.
[12] R.N. Walsh, R.A. Cummins, The Open-Field Test: a critical review, Psychol. Bull. 83 (1976) 482–504.
[13] A.K. Kraeuter, P.C. Guest, Z. Sarnyai, The open field test for measuring locomotor activity and anxiety-like behavior, Methods Mol. Biol. 1916 (2019) 99–103.
[14] K. Kobayashi, N. Shimizu, S. Matsushita, T. Murata, The assessment of mouse spontaneous locomotor activity using motion picture, J. Pharmacol. Sci. 143 (2020) 83–88.
[15] C.M. Larabee, et al., Loss of Nrf2 exacerbates the visual deficits and optic neuritis elicited by experimental autoimmune encephalomyelitis, Mol. Vis. 22 (2016) 1503–1513.
[16] C.K. Glass, K. Saijo, B. Winner, M.C. Marchetto, F.H. Gage, Mechanisms underlying inflammation in neurodegeneration, Cell 140 (2010) 918–934.
[17] S. Brahmachari, Y.K. Fung, K. Pahan, Induction of glial fibrillary acidic protein expression in astrocytes by nitric oxide, J. Neurosci. 26 (2006) 4930–4939.
[18] T.W. West, C. Hess, B.A. Cree, Acute transverse myelitis: demyelinating, inflammatory, and infectious myelopathies, Semin. Neurol. 32 (2012) 97–113.
[19] J.M. Austyn, S. Gordon, F4/80, a monoclonal antibody directed specifically against the mouse macrophage, Eur. J. Immunol. 11 (1981) 805–815.
[20] M.T. Lin, M.F. Beal, Mitochondrial dysfunction and oxidative stress in neurodegenerative diseases, Nature 443 (2006) 787–795.
[21] Y.K. Dhuriya, D. Sharma, Necroptosis: a regulated inflammatory mode of cell death, J. Neuroinflammation 15 (2018) 199.
[22] W. Mandemakers, V.A. Morais, B. De Strooper, A cell biological perspective on mitochondrial dysfunction in Parkinson disease and other neurodegenerative diseases, J. Cell Sci. 120 (2007) 1707–1716.
[23] E. Trushina, C.T. McMurray, Oxidative stress and mitochondrial dysfunction in neurodegenerative diseases, Neuroscience 145 (2007) 1233–1248.
[24] S. Bhaskaran, et al., Neuron-specific deletion of CuZnSOD leads to an advanced sarcopenic phenotype in older mice, Aging Cell 19 (2020), e13225.
[25] K. Sataranatarajan, et al., Neuron specific reduction in CuZnSOD is not sufficient to initiate a full sarcopenia phenotype, Redox Biol. 5 (2015) 140–148.
[26] Y. Su, et al., Deletion of neuronal CuZnSOD accelerates age-associated muscle mitochondria and calcium handling dysfunction that is independent of denervation and precedes sarcopenia, Int. J. Mol. Sci. 22 (2021).
[27] J. Zhan, et al., High speed ventral plane videography as a convenient tool to quantify motor deficits during pre-clinical experimental autoimmune encephalomyelitis, Cells 8 (2019).
[28] J.M.E. Jende, et al., Peripheral nerve involvement in multiple sclerosis: demonstration by magnetic resonance neurography, Ann. Neurol. 82 (2017) 676–685.
[29] R. Boonsuth, et al., Assessing lumbar plexus and sciatic nerve damage in relapsing-remitting multiple sclerosis using magnetisation transfer ratio, Front. Neurol. 12 (2021), 763143.
[30] I. Nikic, et al., A reversible form of axon damage in experimental autoimmune encephalomyelitis and multiple sclerosis, Nat. Med. 17 (2011) 495–499.
[31] F. Lu, et al., Oxidative damage to mitochondrial DNA and activity of mitochondrial enzymes in chronic active lesions of multiple sclerosis, J. Neurol. Sci. 177 (2000) 95–103.
[32] B. Kalman, K. Laitinen, S. Komoly, The involvement of mitochondria in the pathogenesis of multiple sclerosis, J. Neuroimmunol. 188 (2007) 1–12.
[33] H.E. Andrews, P.P. Nichols, D. Bates, D.M. Turnbull, Mitochondrial dysfunction plays a key role in progressive axonal loss in Multiple Sclerosis, Med. Hypotheses 64 (2005) 669–677.
[34] K.G. Su, G. Banker, D. Bourdette, M. Forte, Axonal degeneration in multiple sclerosis: the mitochondrial hypothesis, Curr. Neurol. Neurosci. Rep. 9 (2009) 411–417.
[35] Y. Hou, et al., Ageing as a risk factor for neurodegenerative disease, Nat. Rev. Neurol. 15 (2019) 565–581.
[36] S. Azam, M.E. Haque, R. Balakrishnan, I.S. Kim, D.K. Choi, The ageing brain: molecular and cellular basis of neurodegeneration, Front. Cell Dev. Biol. 9 (2021), 683459.
[37] G.R. Campbell, N. Ohno, D.M. Turnbull, D.J. Mahad, Mitochondrial changes within axons in multiple sclerosis: an update, Curr. Opin. Neurol. 25 (2012) 221–230.
[38] J.L. Zambonin, et al., Increased mitochondrial content in remyelinated axons: implications for multiple sclerosis, Brain 134 (2011) 1901–1913.
[39] D.J. Mahad, et al., Mitochondrial changes within axons in multiple sclerosis, Brain 132 (2009) 1161–1174.
[40] M.E. Witte, et al., Enhanced number and activity of mitochondria in multiple sclerosis lesions, J. Pathol. 219 (2009) 193–204.
[41] M.S. Recks, et al., Early axonal damage and progressive myelin pathology define the kinetics of CNS histopathology in a mouse model of multiple sclerosis, Clin. Immunol. 149 (2013) 32–45.
[42] J. Feng, T. Tao, W. Yan, C.S. Chen, X. Qin, Curcumin inhibits mitochondrial injury and apoptosis from the early stage in EAE mice, Oxid. Med. Cell. Longev. 2014 (2014), 728751.
[43] M. Sadeghian, et al., Mitochondrial dysfunction is an important cause of neurological deficits in an inflammatory model of multiple sclerosis, Sci. Rep. 6 (2016), 33249.

[44] B. Ahn, et al., Mitochondrial oxidative stress impairs contractile function but paradoxically increases muscle mass via fibre branching, J. Cachexia Sarcopenia Muscle. 10 (2019) 411–428.
[45] Y.H. Han, et al., Adipocyte-specific deletion of manganese superoxide dismutase protects from diet-induced obesity through increased mitochondrial uncoupling and biogenesis, Diabetes 65 (2016) 2639–2651.
[46] G.H. Kim, J.E. Kim, S.J. Rhie, S. Yoon, The role of oxidative stress in neurodegenerative diseases, Exp Neurobiol. 24 (2015) 325–340.
[47] G. Schreibelt, et al., Therapeutic potential and biological role of endogenous antioxidant enzymes in multiple sclerosis pathology, Brain Res. Rev. 56 (2007) 322–330.
[48] J. van Horssen, M.E. Witte, G. Schreibelt, H.E. de Vries, Radical changes in multiple sclerosis pathogenesis, Biochim. Biophys. Acta 1812 (2011) 141–150.
[49] K. Newton, G. Manning, Necroptosis and inflammation, Annu. Rev. Biochem. 85 (2016) 743–763.
[50] T.B. Kang, S.H. Yang, B. Toth, A. Kovalenko, D. Wallach, Activation of the NLRP3 inflammasome by proteins that signal for necroptosis, Methods Enzymol. 545 (2014) 67–81.
[51] D. Ofengeim, et al., Activation of necroptosis in multiple sclerosis, Cell Rep. 10 (2015) 1836–1849.
[52] J. Yuan, P. Amin, D. Ofengeim, Necroptosis and RIPK1-mediated neuroinflammation in CNS diseases, Nat. Rev. Neurosci. 20 (2019) 19–33.
[53] K.W. Ko, J. Milbrandt, A. DiAntonio, SARM1 acts downstream of neuroinflammatory and necroptotic signaling to induce axon degeneration, J. Cell Biol. 219 (2020).
[54] M.S. Arrazola, et al., Axonal degeneration is mediated by necroptosis activation, J. Neurosci. 39 (2019) 3832–3844.
[55] M. Onate, et al., The necroptosis machinery mediates axonal degeneration in a model of Parkinson disease, Cell Death Differ. 27 (2020) 1169–1185.
[56] Y. Wang, et al., Necrostatin-1 ameliorates the pathogenesis of experimental autoimmune encephalomyelitis by suppressing apoptosis and necroptosis of oligodendrocyte precursor cells, Exp. Ther. Med. 18 (2019) 4113–4119.
[57] D. Gris, et al., NLRP3 plays a critical role in the development of experimental autoimmune encephalomyelitis by mediating Th1 and Th17 responses, J. Immunol. 185 (2010) 974–981.
[58] S. Malhotra, et al., NLRP3 inflammasome as prognostic factor and therapeutic target in primary progressive multiple sclerosis patients, Brain 143 (2020) 1414–1430.
[59] W. Barclay, M.L. Shinohara, Inflammasome activation in multiple sclerosis and experimental autoimmune encephalomyelitis (EAE), Brain Pathol. 27 (2017) 213–219.
[60] J. Komuczki, et al., Fate-mapping of GM-CSF expression identifies a discrete subset of inflammation-driving T helper cells regulated by cytokines IL-23 and IL-1beta, Immunity 50 (2019) 1289–1304 e1286.
[61] E. Scarpini, et al., IP-10 and MCP-1 levels in CSF and serum from multiple sclerosis patients with different clinical subtypes of the disease, J. Neurol. Sci. 195 (2002) 41–46.
[62] M. Brandes, D.F. Legler, B. Spoerri, P. Schaerli, B. Moser, Activation-dependent modulation of B lymphocyte migration to chemokines, Int. Immunol. 12 (2000) 1285–1292.
[63] M. Krumbholz, et al., Chemokines in multiple sclerosis: CXCL12 and CXCL13 up-regulation is differentially linked to CNS immune cell recruitment, Brain 129 (2006) 200–211.
[64] M.C. Kowarik, et al., CXCL13 is the major determinant for B cell recruitment to the CSF during neuroinflammation, J. Neuroinflammation 9 (2012) 93.
[65] J. Bennett, et al., Blood-brain barrier disruption and enhanced vascular permeability in the multiple sclerosis model EAE, J. Neuroimmunol. 229 (2010) 180–191.
[66] G. Campbell, D.J. Mahad, Mitochondrial dysfunction and axon degeneration in progressive multiple sclerosis, FEBS Lett. 592 (2018) 1113–1121.
[67] S. Faissner, J.R. Plemel, R. Gold, V.W. Yong, Progressive multiple sclerosis: from pathophysiology to therapeutic strategies, Nat. Rev. Drug Discov. 18 (2019) 905–922.
[68] X. Jia, et al., Genome sequencing uncovers phenocopies in primary progressive multiple sclerosis, Ann. Neurol. 84 (2018) 51–63.
[69] S. Zuchner, et al., Mutations in the novel mitochondrial protein REEP1 cause hereditary spastic paraplegia type 31, Am. J. Hum. Genet. 79 (2006) 365–369.
[70] Y. Lim, I.T. Cho, L.J. Schoel, G. Cho, J.A. Golden, Hereditary spastic paraplegia-linked REEP1 modulates endoplasmic reticulum/mitochondria contacts, Ann. Neurol. 78 (2015) 679–696.
[71] P. Young, et al., Single-neuron labeling with inducible Cre-mediated knockout in transgenic mice, Nat. Neurosci. 11 (2008) 721–728.
[72] C.L. Baker Jr., C.L. Baker 3rd, Long-term follow-up of arthroscopic treatment of lateral epicondylitis, Am. J. Sports Med. 36 (2008) 254–260.
[73] R. D'Hooge, et al., Neuromotor alterations and cerebellar deficits in aged arylsulfatase A-deficient transgenic mice, Neurosci. Lett. 273 (1999) 93–96.
[74] S. Bhaskaran, et al., Loss of mitochondrial protease ClpP protects mice from diet-induced obesity and insulin resistance, EMBO Rep. 19 (2018).
[75] K.M. Piekarz, et al., Molecular changes associated with spinal cord aging, Geroscience 42 (2020) 765–784.
[76] M.E. Walsh, et al., Use of nerve conduction velocity to assess peripheral nerve Health in aging mice, J. Gerontol. A Biol. Sci. Med. Sci. 70 (2015) 1312–1319.
[77] G. Krumschnabel, et al., Simultaneous high-resolution measurement of mitochondrial respiration and hydrogen peroxide production, Methods Mol. Biol. 1264 (2015) 245–261.
[78] R. Qaisar, et al., Restoration of sarcoplasmic reticulum Ca(2+) ATPase (SERCA) activity prevents age-related muscle atrophy and weakness in mice, Int. J. Mol. Sci. 22 (2020).
[79] R. Qaisar, et al., Restoration of SERCA ATPase prevents oxidative stress-related muscle atrophy and weakness, Redox Biol. 20 (2019) 68–74.
[80] L.K. Hill, et al., Detection of cerebrovascular loss in the normal aging C57bl/6 mouse brain using in vivo contrast-enhanced magnetic resonance angiography, Front. Aging Neurosci. 12 (2020), 585218.